Multi–Frequency and Multi–Polarization Synthetic Aperture Radar for the Larsen–C A–68 Iceberg Monitoring

Ferdinando Nunziata[1], Andrea Buono[1], Miguel Moctezuma[2], Flavio Parmiggiani[3], Giuseppe Aulicino[4], Maurizio Migliaccio[1]

[1]*Dipartimento di Ingegneria, Università degli Studi di Napoli Parthenope,* Napoli, Italy
{ferdinando.nunziata, andrea.buono, maurizio.migliaccio}@uniparthenope.it

[2]*Facultad de Ingeniería, Universidad Nacional Autónoma de México,* Mexico City, Mexico
miguelm@verona.fl–p.unam.mx

[3]*Istituto di Scienze dell'Atmosfera e del Clima, Consiglio Nazionale delle Ricerche,* Bologna, Italy
f.parmiggiani@isac.cnr.it

[4]*Dipartimento di Scienze della Vita e dell'Ambiente, Università Politecnica delle Marche,* Ancona, Italy
g.aulicino@staff.univpm.it

***Abstract*—Since 2016 the fracture of the Larsen–C ice shelf has been regularly observed in the Eastern Weddell Sea (68°S, 61°W, Antarctica). This process led to the final collapse in July 2017, when an area of about 6000 km^2 (i. e., about 9–12% of the whole shelf) was lost. In this study the resulting calved iceberg, termed as "A–68" from the U. S. National Ice Center, is observed using multi–frequency and multi–polarization Synthetic Aperture Radar (SAR) satellite platforms that include L–band Alos PalSAR–2, C–band Sentinel–1 and X–band COSMO–SkyMed. A large set of SAR scenes were considered, collected in ScanSAR imaging modes over a time span of about 1 year, to analyze the iceberg properties and its melting process and drifting.**

***Index Terms*—SAR, polarization, segmentation, iceberg, Larsen ice shelf**

I. Introduction

The iceberg "A–68", whose surface area and weight are about 6000 km^2 and one trillion tonnes, respectively, calved from the Larsen–C ice shelf in the Eastern Weddell Sea (68°S 61°W, Antarctica) in July 2017. It is one of the largest icebergs ever recorded, whose calving reduced the overall size of the Larsen–C ice shelf by about 9–12% (see Fig. 1).

The fracture of the Larsen–C Ice Shelf and the corresponding origin of the giant tabular iceberg have been continuously monitored since 2016 with particular interest to the possible worrisome evolution for climate change, sea level rise, safe navigation, etc. [1], [2].

In this context, a continuous, updated and effective monitoring of polar regions is ensured by satellite Synthetic Aperture Radar (SAR) instruments that provide useful imagery characterized by fine resolution (up to few meters), dense revisit time (up to few days) and wide area coverage (up to hundreds kilometers). In addition, the SAR capability of transmitting microwave radiations allows observing polar regions almost independently on weather conditions (clouds, rain cells, etc.) and solar illumination. In this study, the potential of spaceborne SAR sensors to support the Larsen–C A–68 iceberg monitoring, i. e., detection and tracking, is addressed. The analysis is undertaken according to single–polarization intensity (HH, horizontal transmit/horizontal receive) and topological parameters used to define a set of linear functions for iceberg recognition [3], and to dual–polarization intensity (HH and HV, horizontal transmit/vertical receive) to

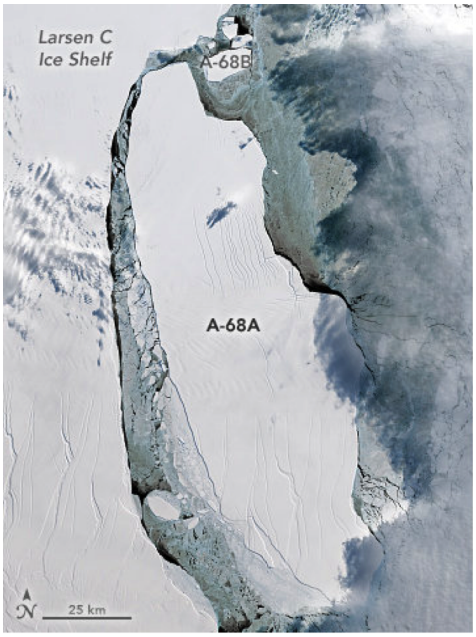

Fig. 1. Study area that includes the "A–68" iceberg calved from the Larsen–C ice shelf. Credit to Joshua Stevens (Landsat data are from the U.S. Geological Survey).

This study was partly supported by the EU SPICES project (www.h2020-spices.eu/), by the Direccion General de Asuntos del Personal Acadèmico and the Coordinacion de Estudios de Posgrado, UNAM, and by the Università di Napoli Parthenope under the project ID DING 118.

evaluate the coherent versus incoherent scattering contribution [4], [5].

When dealing with iceberg detection, different segmentation algorithms have been proposed and validated on C– and X–band SAR imagery that are based on constant false alarm rate (CFAR), watershed and finite mixture model [6]–[8]. When dealing with iceberg drift tracking, Global Positioning System (GPS) buoys deployed on the icebergs can be used [9], [10]. In addition, when dual–polarization information is available, the iceberg/clutter contrast can be enhanced to improve segmentation and additional information on the scattering properties of the icebergs can be inferred [11], [12].

In this study, two different approaches for the Larsen–C A–68 iceberg monitoring are presented. A first method is developed that exploits the inherent random nature of the SAR imagery, i. e., functional methods to regularize the distribution of the pixel–wise scatterers and, therefore, to implement automatic segmentation, can be accomplished, according to the stochastic process theory, by using energy function representations through the Markov Random Fields (MRFs) [13]. A second techniques is also proposed that exploits the power ratio between the coherent and incoherent received signals, namely the Rice factor (RF), to distinguish regions resulting in coherent bacskcatter from areas that result in an incoherent backscattering [4], [5]. The proposed methodology is implemented according to the following steps: i) speckle filtering, ii) stochastic segmentation, iii) multi–polarization evaluation of RF and iv) estimation of the geographic position of the iceberg centroid and total surface area.

II. Methodology

In this section, the theoretical rationale that lies at the basis of the proposed analysis is presented.

A. MRF segmentation

SAR imagery is speckled; hence, a preliminary step consists of de–speckling. Then, segmentation is undertaken.

Speckle is a random inherent process that represents a multiplicative noise in SAR imagery [14]. The latter must be filtered out in order to make image features suitable for the subsequent segmentation process. In this study, two different kinds of elements must be integrated, i. e., open–sea and ice–covered objects. Their different morphological properties are preserved during the speckle filtering by using the non–linear algorithm proposed in [15]. The gray–scale morphological reconstruction of the intensity patterns consists of applying erosion (E) and dilation (D) operations as follows:

$$k_{i+1} = D[k_i, b] \cap f \quad , \tag{1}$$

where i is the finite index of the number of morphological operations, f is a mask, b is a flat disk–shaped structuring element defined by a 3-pixels radius and the image $f_m \subset f$ is a marker such that $k_1 = f_m$. The erosion of the original image by b produces the primary marker image, i.e., $f_m = E[f,b]$. The iterative dilation method described in eq. (1) results in the final reconstruction R_f $(f_m) = k_N$, where N is the number of the last dilation operation. As a result, the iterative dilation by a 8–pixels connectivity matrix removes gray–level features smaller than b while preserving geometric shapes.

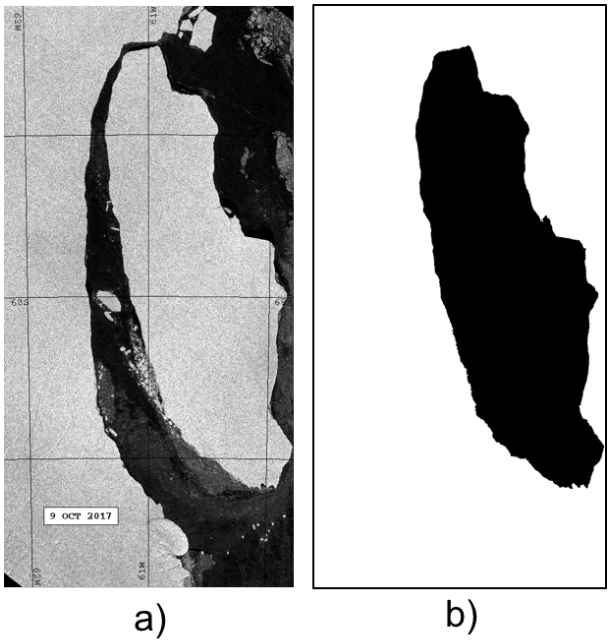

Fig. 2. Example of the CSK SAR imagery collected on October 9, 2017 over the region of the A–68 iceberg. a) HH–polarized NRCS; b) MRF–based segmentation output.

The second step consists of stochastic segmentation. When dealing with Markovian stochastic segmentation, significantly uncertainty may be in place due to the fact that a given pixel, according to the probability distribution classification criteria, may have attributes that belong to more than one class. In this study, a fuzzy c–means (FCM) approach is adopted in order to overcome this issue [16]. The cost function that needs to be optimized is iteratively implemented by a n–dimensional set of parameters p_j, where n is the number of clusters:

$$J(P, M) = \sum_{i=1}^{m} \sum_{j=1}^{n} (M_{ij})^c ED(x_i - p_j) \quad , \tag{2}$$

where x_i is the pixel under test within the cluster C_j defined by a variable M_{ij} belonging to the range 0 – 1 ($\sum_{j=1}^{n} M_{ij} = 1$), m is the total number of pixels of the input image, c is the fuzzy–paramater and ED is the Euclidean distance. No more than 54 iterations are required to ensure the FCM convergence when $c = n = 2$.

The segmentation rule is based on the Bayes decision $P(W_j/X) = P(X,W_j)/P(X)$ with $P(X,W_j) = P(X/W_j)$ $P(W_j)$, where X is the original image. The term $P(X/W_j)$ is derived from eq. (2) in order to ensure that the membership variable M_{ij} approaches the modes of the conditional probability distribution approach, i. e., $P(X/W_j, \mu_j) \approx M_{ij}$ where μ_j is the mean value of the jth cluster. Then, a contextual segmentation criterion based on the maximum–likelihood estimator is adopted to obtain a homogeneous fields.

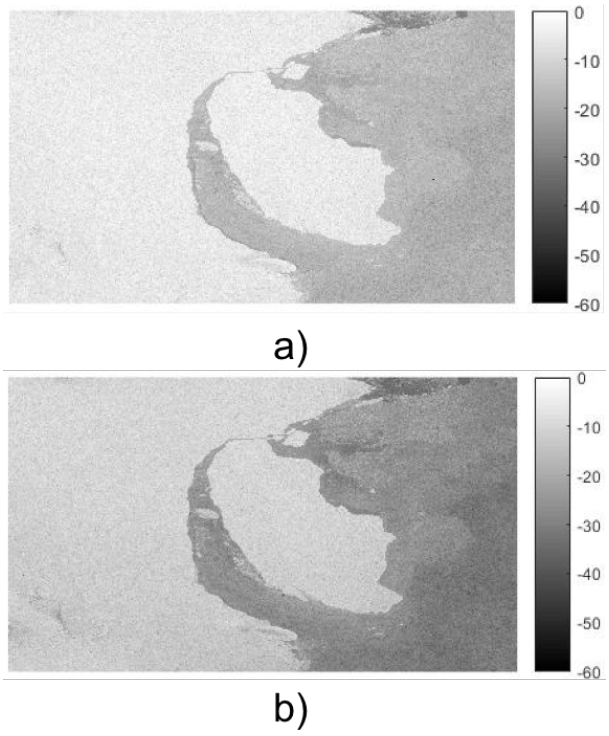

Fig. 3. Alos PalSAR–2 SAR imagery collected on October 27, 2017 over the region of the A–68 iceberg. a) HH and b) HV–polarized NRCS.

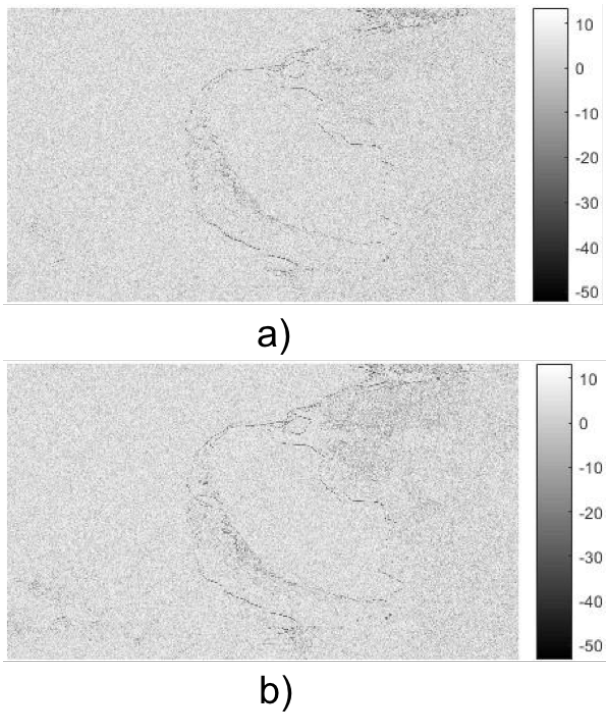

Fig. 4. Rice factor imagery: a) HH channel; b) HV channel.

The Bayesian estimation of the fields X and W, assumed to be realizations of MRFs, follows a Gibb exponential distribution that results in energy functions given by:

$$\hat{W} = min_x[U(W|X)] \approx min_x[U(X|W) + U(W)] \quad , \quad (3)$$

where $\hat{W}$ is the estimated label field. Hence, by combining FCM and a MRF–based stochastic relaxation scheme in a semi–supervised segmentation algorithm where the range of the label field is the only paramater to be tuned since FCM provides to the MRF segmentation stage the probability low abstraction needed to define the radiometric distribution of the scene elements.

B. Rice factor approach

The RF is given by the power ratio between the coherent and incoherent received signals [4], [5]. In this study we exploit RF to distinguish regions resulting in coherent bacskcatter from areas that result in an incoherent backscattering.

To expedite time processing, the SAR image is partitioned into $NI \times NI$ pixels wide tiles that are used to estimate incoherent power. Within each tile, a moving local window is applied to evaluate the coherent power over a $NC \times NC$ pixels region. These two powers are then compared to evaluate RF:

$$RF = \frac{\langle \sigma^o \rangle^2_{NC}}{2\text{std}[\sigma^o]^2_{NI}}, \quad (4)$$

where σ^o is the calibrated Normalized Radar Cross Section (NRCS), $\langle \cdot \rangle$ stands for ensemble average operator that, in this study, is replaced by a boxcar spatial averaging window whose size is NC and NI for the estimation of the coherent and incoherent components, respectively. The dimension of the local window (NC) is set to minimize the unavoidable decrease of the native image resolution and to allow a better detection of the small icebergs, while the dimension of the tiles (NI) is set to get a stable reference background level.

III. Experiments

In this section a multi–polarization analysis is undertaken on a SAR data set collected over the A–68 iceberg area. Scenes collected by different SAR platforms at different polarizations and frequencies are considered; i.e.; L–band Alos PalSAR–2 in dual–polarimetric HH–HV mode, C–band Sentinel–1 in dual–polarimetric HH–HV/VV–VH mode and X–band COSMO–SkyMed (CSK) in HH–polarized single–polarization mode.

MRF analysis consists of speckle filtering and segmentation, aiming at generating a binary output that can be further processed to extract the geographic position of the centroid and the area of the iceberg. Although a time series of SAR imagery has been processed, in this study segmentation results are only shown for the CSK SAR scene collected on October 9, 2017 over the area of interest. An excerpt of the HH–polarized NRCS image is shown in Fig. 2 a) while the MRF segmentation output is shown in Fig. 2 b). By processing the whole time series consisting of SAR scenes collected from July 19 up to December 7, 2017, information on the iceberg

position and its area can be discussed against time evolution. The area of the iceberg is around 5760 km^2 at the beginning of the time series; while it reduces up to 5630 km^2 at the end. However, it was also noted that the area is not a monotonic function of the time but it exhibits fluctuations that are likely due to ice fragments that may attach to the main iceberg. The drifting associated to the iceberg resulted in an Eastbound displacement of about 28 km.

To analyze value–added information that can be extracted from dual–polarimetric SAR imagery, RF is estimated from the dual–polarimetric HH–HV SAR image collected by Alos PalSAR–2 on October 27, 2017, whose excerpts are shown in Fig. 3 a) and b), respectively.

It can be noted that the iceberg is well–visible in both channels. Note also that, although the two channels result in a different backscattered intensity level with the HH one being almost everywhere larger than the HV one, similar patterns can be identified in both channels.

RF is evaluated using both channels and results are shown in Fig. 4 a) and b). Both RF images clearly show the contours associated to the icebergs that are characterized by RF values lower than the iceberg and the mainland. Lower RF values apply also over the sea area witnessing that a very incoherent behavior applies. A simple threshold equal to -10 dB has been empirically set to obtain the binary output shown in Fig. 5.

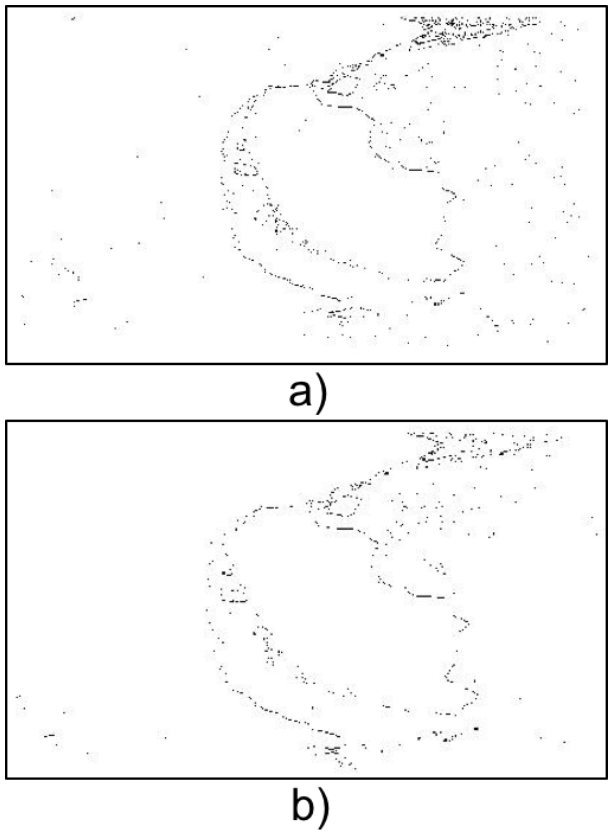

Fig. 5. Rice factor binary imagery: a) HH channel; b) HV channel.

The latter clearly shows that iceberg's edge can be straightforwardly extracted using simple image processing techniques.

IV. Conclusions

In this study the Larson–C A–68 iceberg is analyzed using multi–frequency and multi–polarization SAR data to extract useful information to monitor the iceberg evolution. Two segmentation techniques are proposed based on MRF and RF, respectively. Both the methods succeed to extract iceberg's edges.

Acknowledgment

Cosmo–SkyMed SAR data were delivered under an Italian Space Agency licence to use in the framework of "COSMO–SkyMed Open Call for Science Initiative" (ID 237).

Alos–PalSAR 2 SAR data were provided under the "6th Japan Aerospace Exploration Agency/Earth Observation Research Center Research Announcement" (ID 3064).

References

[1] NASA, "Rift in Antarcticas Larsen C ice Shelf", *www.nasa.gov/image-feature/rift-in-antarcticas-larsen-c-ice-shelf*, 2017. Accessed on 30/03/2018.

[2] B. Kulessa, D. Jansen, A. J. Luckman, E. C. King, and P. R. Sammonds, "Marine ice regulates the future stability of a large Antarctic ice shelf", *Nature Communications*, vol. 5, no. 3707, pp. 354–366, 2014.

[3] A. K. Mazur, A. K. Wahlin, and A. Krezel, "An object–based SAR image iceberg detection algorithm applied to the Amundsen Sea", *Remote Sensing of Environment*, vol. 189, pp. 67 – 83, 2017.

[4] M. Migliaccio, G. Ferrara, A. Gambardella, F. Nunziata, and A. Sorrentino, "A physically consistent speckle model for marine SLC SAR images," *IEEE J. Ocean. Eng.*, vol. 32, no. 4, pp. 839848, Oct. 2007.

[5] A. Gambardella, F. Nunziata and M. Migliaccio, "A Physical Full-Resolution Ship Detection Filter," *IEEE Geosci. Remote Sens. Lett.*, vol. 5, no. 4, 2008.

[6] A. Frost, R. Ressel, and S. Lehner, "Automated Iceberg Detection Using High-Resolution X-Band SAR Images", *Canadian Journal of Remote Sensing*, vol. 42, no. 4, pp. 354–366, 2016.

[7] T. A. M. Silva and G. R. Bigg, "Computer–based identi
cation and tracking of Antarctic icebergs in SAR images", *Remote Sensing of Environment*, vol. 94, no. 3, pp. 287–297, 2005.

[8] V. Akbari and C. Brekke, "Iceberg Detection in Open and Ice–Infested Waters Using C–Band Polarimetric Synthetic Aperture Radar", *IEEE Transactions on Geoscience and Remote Sensing*, vol. 56, no. 1, pp. 407–421, 2018.

[9] C. Wesche and W. Dierking, "Estimating iceberg paths using a wind–driven drift model", *Cold Regions Science and Technology*, vol. 125, Supplement C, pp. 31–39, 2005.

[10] R. Yulmetov, A. Marchenko, and S. Loset, "Iceberg and sea ice drift tracking and analysis o north–east Greenland", *Ocean Engineering*, vol. 123, Supplement C, pp. 223–237, 2016.

[11] A. Marino, W. Dierking, and C. Wesche, "A Depolarization Ratio Anomaly Detector to Identify Icebergs in Sea Ice Using Dual–Polarization SAR Images", *IEEE Transactions on Geoscience and Remote Sensing*, vol. 54, no. 9, pp. 5602–5615, 2016.

[12] F. Nunziata, A. Buono, M. F. Moctezuma, F. Parmiggiani, and M. Migliaccio, "Observations of Terra Nova Bay polynya by Radarsat–2: comparison of dual– with single–polarization segmentation performances", *RTSI 2017 – IEEE 3rd International Forum on Research and Technologies for Society and Industry, Conference Proceedings*, Modena, Italy, 11–13 September, 2017.

[13] A. Papoulis and S. U. Pillai, "Probability, Random Variables, and Stochastic Processes", *4th ed. New York, NY USA, McGraw-Hill Higher Education*, 2002..

[14] H. Maitre, "Processing of Synthetic Aperture Radar (SAR) images", *ISTE. Hoboken, NJ: Wiley*, 2010.

[15] R. C. Gonzalez and R. E. Woods, "Digital Image Processing", *3rd ed. Upper Saddle River, NJ, USA: Prentice-Hall, Inc.*, 2007.

[16] R. O. Duda, P. E. Hart, and D. G. Stork, "Pattern Classification", *2nd ed. Wiley-Interscience*, 2000.